EPJ Web of Conferences **102**, 00015 (2015)
DOI: 10.1051/epjconf/201510200015

Ionization and heating by X-rays and cosmic rays*

Manuel Güdel

[1] *Department of Astrophysics, University of Vienna, Türkenschanzstrasse 17, 1180, Vienna, Austria*

Abstract. High-energy radiation from the central T Tauri and protostars plays an important role in shaping protoplanetary disks and influences their evolution. Such radiation, in particular X-rays and extreme-ultraviolet (EUV) radiation, is predominantly generated in unstable stellar magnetic fields (e.g., the stellar corona), but also in accretion hot spots. Even jets may produce X-ray emission. Cosmic rays, i.e., high-energy particles either from the interstellar space or from the star itself, are of crucial importance. Both high-energy photons and particles ionize disk gas and lead to heating. Ionization and heating subsequently drive chemical networks, and the products of these processes are accessible through observations of molecular line emission. Furthermore, ionization supports the magnetorotational instability and therefore drives disk accretion, while heating of the disk surface layers induces photoevaporative flows. Both processes are crucial for the dispersal of protoplanetary disks and therefore critical for the time scales of planet formation. This chapter introduces the basic physics of ionization and heating starting from a quantum mechanical viewpoint, then discusses relevant processes in astrophysical gases and their applications to protoplanetary disks, and finally summarizes some properties of the most important high-energy sources for protoplanetary disks.

1 Introduction

Protostellar and protoplanetary disks are immersed in various types of high-energy radiation and particle fluxes. Among them figure most prominently extreme-ultraviolet and X-ray radiation from the magnetized stellar corona of the central star and in some cases from collimated jets; hard X-rays and gamma-rays from stellar flares; interstellar X-rays from neighboring stars in stellar clusters or from distributed hot plasma in star-forming regions; and galactic cosmic rays and energetic particles ejected during stellar flares ("stellar cosmic rays"). High-energy radiation and cosmic rays modify cold protostellar disk gas primarily due to their ionization power. In the process of ionizing disk gas, the upper layers of the disk are also heated to temperatures of up to several thousand K. Both temperature gradients and ionized species drive a plethora of chemical reactions that would be impossible in the absence of high-energy sources. Ionization and heating are also prime agents of disk destruction: the former by possibly inducing the magnetorotational instability (MRI) through coupling of ionized disk gas to magnetic fields, and the latter by photoevaporating gas from the uppermost layers of the disk. The disk lifetime may thus well be controlled by high-energy processes taking place on or near the central star.

* 14th Lecture from Summer School "Protoplanetary Disks: Theory and Modelling Meet Observations"

In this chapter, I first outline some basic theory of ionization and heating. I will then present selected methodology for application to astrophysical gases. The subsequent sections will discuss applications of X-ray and cosmic-ray irradiation of protoplanetary disks and show results pertaining to the disk ionization degree, the temperature structure, the magnetorotational instability, photoevaporation of disk material, and chemical processing. Finally, I will summarize our knowledge about the ionizing sources themselves.

2 Quantum Mechanical Treatment of Photoionization

A full understanding of photoelectric absorption and photoionization requires a quantum mechanical treatment of radiation processes. I summarize here the principal steps leading to the photoionization cross section. Extensive treatments can be found, e.g., in Rybicki & Lightman (1979), Shu (1991), or Kahn (2005).

The wave function $\psi(\mathbf{x}, t)$ of an electron is the probability amplitude for the electron (e.g., bound in an atom) to be located at x at time t. It obeys the *Schrödinger equation,*

$$i\hbar\frac{\partial\psi}{\partial t} = H\psi, \tag{1}$$

where H is the Hamiltonian associated with the energy of the system. For a time-independent Hamiltonian, the *time-independent Schrödinger equation*

$$H\psi_j = E_j\psi_j \tag{2}$$

is used to find the stationary states ("eigenstates") ψ_j with energy E_j (the eigenvalues of the equation).

Quantum mechanics describes interactions of radiation ("photons") with particles in terms of a change of quantum state, described by matrix elements $\langle f|H|i\rangle$ involving an initial state $|i\rangle$, a final state $|f\rangle$, and a "perturbing Hamiltonian" associated with the external radiation field.

To find H for the system, we start with the classical Euler-Lagrange equation

$$\frac{\mathrm{d}}{\mathrm{d}t}\left(\frac{\partial L}{\partial\dot{\mathbf{x}}}\right) = \frac{\partial L}{\partial\mathbf{x}}. \tag{3}$$

The *Lagrangian* L of a particle in an electromagnetic field reads

$$L = \frac{1}{2}m|\dot{\mathbf{x}}|^2 - q\varphi(\mathbf{x}, t) + \frac{q\dot{\mathbf{x}}}{c}\mathbf{A}(\mathbf{x}, t). \tag{4}$$

The first two terms express the kinetic and the potential energy; φ and $\mathbf{A}$ are, respectively, the scalar and vector potentials (The above L leads to the correct equation of motion of the particle in a field). In what follows, we are using the *Coulomb gauge*, i.e., $\nabla\cdot\mathbf{A} = 0$. The Hamiltonian follows from L and the *canonical momentum* $p = \partial L/\partial\dot{\mathbf{x}}$ as

$$\begin{aligned} H = \dot{\mathbf{x}}\mathbf{p} - L &= \frac{1}{2m_\mathrm{e}}\left|\mathbf{p} - \frac{q}{c}\mathbf{A}(\mathbf{x}, t)\right|^2 + q\varphi(\mathbf{x}, t) \\ &= \frac{1}{2m_\mathrm{e}}|\mathbf{p}|^2 - \frac{q}{2mc}(\mathbf{p}\cdot\mathbf{A} + \mathbf{A}\cdot\mathbf{p}) + \frac{q^2}{2mc^2}\mathbf{A}\cdot\mathbf{A} + q\varphi(\mathbf{x}, t). \end{aligned} \tag{5}$$

For the electron, we now set $q = -e$ and $m = m_\mathrm{e}$. We separate H into three terms,

$$H_0 = \frac{1}{2m_\mathrm{e}}|\mathbf{p}|^2 - e\varphi(\mathbf{x}), \qquad H_1 = \frac{e}{2m_\mathrm{e}c}(\mathbf{p}\cdot\mathbf{A} + \mathbf{A}\cdot\mathbf{p}), \qquad H_2 = \frac{e^2}{2m_\mathrm{e}c^2}\mathbf{A}\cdot\mathbf{A}. \tag{6}$$

These Hamiltonians describe the electronic equilibrium state of the atom (static H_0), perturbations due to one-photon interactions (H_1) and two-photon interactions (H_2). It is easy to show that the relative importance of the three terms is, e.g. for a hydrogen atom, $H_2/H_1 \sim a_0^2\mathcal{E}/e$ and $H_1/H_0 \sim a_0^2\mathcal{E}/e$, the ratio of the electric field ($\mathcal{E}$) of the radiation field to the Coulomb field at one Bohr radius a_0. This ratio is usually $\ll 1$ (e.g., Shu 1991). We therefore neglect H_2 for two-photon processes in the following.

We introduce quantum-mechanical treatment by identifying $\mathbf{p}$ with the quantum mechanical operator $-i\hbar\nabla$, thus writing the Hamiltonian terms H_0 and H_1 as

$$H_0 = -\frac{\hbar^2}{2m_e}\nabla^2 - e\varphi(\mathbf{x}), \qquad H_1 = -\frac{ie\hbar}{m_e c}\mathbf{A}\cdot\nabla \tag{7}$$

where we have used $\mathbf{A}\cdot\mathbf{p} = \mathbf{p}\cdot\mathbf{A}$ for H_1 because $\nabla\mathbf{A} = 0$. We assume a monochromatic plane wave and therefore write the vector potential as

$$\mathbf{A}(\mathbf{x},t) = \mathrm{Re}\left(\mathbf{A}_0 e^{i(\mathbf{kx}-\omega t)}\right) = \frac{1}{2}|\mathbf{A}_0|\left(\hat{\epsilon}e^{i(\mathbf{kx}-\omega t)} + \hat{\epsilon}^* e^{-i(\mathbf{kx}-\omega t)}\right) \tag{8}$$

where $\hat{\epsilon}$ is the polarization vector of the wave. The time-averaged Poynting vector of the radiation field is

$$< S > = \frac{c}{4\pi}|\mathcal{E}(t)|^2\hat{k} = \frac{\omega^2}{8\pi c}|A_0|^2\hat{k} \tag{9}$$

where $\mathcal{E}$ is the wave electric field and $\hat{k}$ is the unit vector in the propagation direction of the wave. The Poynting energy flux $| < S > |$ can also be expressed in terms of discrete-photon flux through area F, $dN/dFdt$:

$$\frac{\mathrm{d}N}{\mathrm{d}F\mathrm{d}t} = \frac{| < S > |}{\hbar\omega} = \frac{\omega}{8\pi\hbar c}|\mathbf{A}_0|^2. \tag{10}$$

Returning to the Hamiltonian, the static part H_0 describes the structure of the stationary states of the atom. From the Schrödinger equation, we see that the energy eigenstates follow the time dependence

$$\psi_j(\mathbf{x},t) = \varphi_j(\mathbf{x})e^{-iE_j t/\hbar}. \tag{11}$$

Any wave function $\psi(\mathbf{x},t)$ for the atomic system (bound or free) can be expanded by the complete basis defined by all eigenfunctions $\varphi_j(\mathbf{x})$. Because H_1 can be considered a small perturbation of H, we therefore write,

$$\psi(\mathbf{x},t) = \sum_j c_j\varphi_j(\mathbf{x})e^{-iE_j t/\hbar} \tag{12}$$

with the normalization condition $\int\psi(\mathbf{x},t)\psi^*(\mathbf{x},t)d^3x \equiv \langle\psi|\psi\rangle = 1$. We now substitute this expansion into the time-dependent Schrödinger equation to find

$$\sum_j c_j H_1\varphi_j e^{-iE_j t/\hbar} = i\hbar\sum_j \dot{c}_j\varphi_j e^{-iE_j t/\hbar} \tag{13}$$

where we have subtracted the zero-order terms involving $H_0\sum_j ... = \sum_j E_j ....$ Eq. 13 is a differential equation system for the time-dependent coefficients c_j. The initial condition is that for $t = 0$, the system is in an eigenstate $\varphi_i(\mathbf{x})$:

$$\psi(\mathbf{x},0) = \varphi_i(\mathbf{x}). \tag{14}$$

We multiply the above equations with $\varphi_f^* e^{iE_f t/\hbar}$ defining a possible final state, and integrate over all $\mathbf{x}$. For simplicity, we now change to the Dirac notation:

$$\sum_j c_j e^{i(E_f-E_j)t/\hbar}\langle\varphi_f|H_1|\varphi_j\rangle \equiv \sum_j c_j e^{i(\omega_f-\omega_j)t}\langle\varphi_f|H_1|\varphi_j\rangle = i\hbar\dot{c}_f \tag{15}$$

where we have set $\omega_{f,j} \equiv E_{f,j}/\hbar$, and on the RHS we note that $\langle\varphi_f|\varphi_j\rangle = \delta_{fj}$ for the orthonormal set of eigenfunctions φ_j. The initial condition 14 is equivalent to $c_j = \delta_{ji}$ at $t = 0$. We iterate the perturbation starting at $t = 0$, therefore setting $j = i$ and integrating in t:

$$c_f(t) = \frac{1}{i\hbar}\int_0^t \langle\varphi_f|H_1|\varphi_i\rangle e^{i(\omega_f-\omega_i)t}\mathrm{d}t, \tag{16}$$

an iteration that is sufficient for our purposes. Note that the perturbation Hamiltonian H_1 in Eq. 16 has terms proportional to $e^{+i(\mathbf{kx}-\omega t)}$ and $e^{-i(\mathbf{kx}-\omega t)}$ (i.e., $H_1(t) = \bar{H}e^{\pm i\omega t}$), leading to

$$c_f(t) = \frac{1}{i\hbar}\langle\varphi_f|\bar{H}_1|\varphi_i\rangle\int_0^t e^{i(\omega_f-\omega_i\pm\omega)t}\mathrm{d}t = -\frac{1}{\hbar}\langle\varphi_f|\bar{H}_1|\varphi_i\rangle\frac{e^{i(\omega_f-\omega_i\pm\omega)t}-1}{\omega_f-\omega_i\pm\omega} \tag{17}$$

Recall that in quantum mechanics, $|c_f(t)|^2$ (equal to the absolute square of the wave function) gives the probability that the system is now, at time t, in its final state f. The transition *rate* is therefore

$$R = \lim_{t\to\infty}\frac{|c_f(t)|^2}{t} = \frac{2\pi}{\hbar^2}|\langle f|\bar{H}_1|i\rangle|^2\delta(\omega_f-\omega_i\pm\omega) = \frac{2\pi}{\hbar}|\langle f|\bar{H}_1|i\rangle|^2\delta(E_f-E_i\pm\hbar\omega). \tag{18}$$

(Kahn 2005) where δ stands for the "delta" distribution. We immediately see that a transition requires emission or absorption of an energy quantum $\hbar\omega$ that is (for $t\to\infty$) equal to the energy difference $E_f - E_i$. If $E_f > E_i$, then $\hbar\omega < 0$, which represents an absorption of a photon from the electromagnetic field. Using our H_1 in Eq. 7 and $\mathbf{A}$ from Eq. 8, we find

$$R = \frac{\pi\hbar e^2}{2m_e^2c^2}|A_0|^2|\langle f|e^{\pm i\mathbf{kx}}\hat{\epsilon}^{(*)}\cdot\nabla|i\rangle|^2\delta(E_f-E_i\mp\hbar\omega) \tag{19}$$

(the upper sign and $\hat{\epsilon}$ for absorption, the lower sign and $\hat{\epsilon}^*$ for emission).

Assume now that $|\varphi_i\rangle$ is a bound state and $|\varphi_f\rangle$ is a free state. For the total transition rate, we integrate over all f states (i.e., all possible $\mathbf{p}$). By the uncertainty principle, a particle cannot be localized in a phase space volume less than $\mathrm{d}^3\mathbf{x}\mathrm{d}^3\mathbf{p} = (2\pi\hbar)^3$. The density of free states is therefore ($E = mv^2/2 \to p = \sqrt{2mE}$)

$$n(E)\mathrm{d}E = \frac{V\mathrm{d}^3\mathbf{p}}{(2\pi\hbar)^3} = \frac{Vm(2mE)^{1/2}\mathrm{d}E\mathrm{d}\Omega}{(2\pi\hbar)^3}. \tag{20}$$

We write for the final, free state of the electron

$$\varphi_f(\mathbf{x}) = \frac{1}{V^{1/2}}e^{-i\mathbf{p}_f\mathbf{x}/\hbar} \tag{21}$$

(so that $\langle\psi_f|\psi_f\rangle = 1$ if integrated over the allowable volume). Integrating the transition rate R over all energies of the final states, using the density of states $n(E)$, yields

$$\mathrm{d}R = \frac{1}{4}\frac{e^2}{(2\pi\hbar c)^2}v_f|\mathbf{A}_0|^2|\langle e^{-i\mathbf{p}_f\mathbf{x}/\hbar}|e^{\pm i\mathbf{kx}}\hat{\epsilon}\cdot\nabla|i\rangle|^2\mathrm{d}\Omega \tag{22}$$

(where $mv_f = (2mE_f)^{1/2}$) and therefore the differential cross section

$$\frac{\mathrm{d}\sigma}{\mathrm{d}\Omega} = \frac{\mathrm{d}R/\mathrm{d}\Omega}{\mathrm{d}N/\mathrm{d}t\mathrm{d}F} = \frac{\mathrm{d}R/\mathrm{d}\Omega}{\omega|\mathbf{A}_0|^2/(8\pi\hbar c)} = \frac{e^2v_f}{2\pi\hbar c\omega}\left|\langle e^{-i\mathbf{p}_f\mathbf{x}/\hbar}|e^{\pm i\mathbf{kx}}\hat{\epsilon}\cdot\nabla|i\rangle\right|^2. \tag{23}$$

Let us now apply this theory to the concrete situation in which a K shell electron of a hydrogen-like atom is liberated to a free state via photoionization. We write for the initial state, including normalization,

$$\varphi_i = \frac{1}{(\pi a_Z^3)^{1/2}} e^{-|\mathbf{x}|/a_Z} \tag{24}$$

where $a_Z = \hbar^2/(Zm_e e^2)$ corresponds to the "Bohr radius" for a nucleus of charge Z. A lengthy calculation for the integration in Eq. 22 yields a transition rate (Shu 1991)

$$R = \frac{8\pi e^2 a_Z^3}{3V\hbar m_e^2 c^3} \omega^{-3} \mathcal{N}(\omega)(\hbar k_e)^2 \left(\frac{\hbar}{m_e a_Z^2}\right)^4 \tag{25}$$

where $\mathcal{N}(\omega)$ is the photon occupation number for frequency ω. For the photoionization cross section out of the nth shell in a hydrogen-like ion is

$$\sigma_n(\omega) = \frac{64\alpha}{3\sqrt{3}} \frac{Z^4}{n^5} \left(\frac{1\ Ry}{\hbar\omega}\right)^3 \pi a_0^2 g \approx \text{const} \frac{Z^4}{n^5 \omega^3} \quad [\text{cm}^2] \tag{26}$$

where the fine structure constant $\alpha = e^2/(\hbar c) \approx 1/137$, the Bohr radius $a_0 = \hbar^2/(m_e e^2) \approx 5.3 \times 10^{-9}$ cm, and $1Ry = m_e e^4/(2\hbar^2) = 13.6$ eV, and g is a Gaunt factor of order unity. This important result shows that the cross section is largest for $n = 1$ (inner shell), and also strongly depends on the atomic number, Z. Furthermore, the cross section is largest at the ionization edge and drops like ω^3.

Many-electron atoms show a series of ionization edges as they lose electrons from successive shells - see Fig. 1. For the most important cosmic elements, these edges are located between 13.6 eV for hydrogen (the H Lyman edge) and 7.1 keV for Fe. X-rays below ≈ 7 keV and extreme-ultraviolet radiation therefore suffer from absorption as they propagate through interstellar space, with relevant equivalent hydrogen column densities of $N_{\rm H} \approx 7.5 \times 10^{23}$ cm^{-2} for $\tau = 1$ at 7 keV, $N_{\rm H} \approx 4 \times 10^{21}$ cm^{-2} for 1 keV, or $N_{\rm H} \approx 2 \times 10^{19}$ cm^{-2} for 0.1 keV. This interstellar or circumstellar matter absorbs EUV and soft E-rays first, while the photoionization cross section rapidly decreases for increasing photon energy due to the ν^{-3} dependence of the cross section. Beyond the Fe K edge, photons encounter only the rapidly decaying tail of the K-edge cross section. Measuring EUV/X-ray absorption therefore provides an important method to estimate (near-neutral) gas column densities along the line of sight to the source.

By implication, softer X-rays are more efficient agents of ionization than hard photons although due to the larger optical depth, ionization occurs closer to the "surface" of an obstacle such as a protoplanetary disk for softer photons. Harder X-ray photons penetrate into deeper, cooler layers of the disk, while the hardest photons eventually cross the entire disk without absorption. It follows that photoionization is locally dominated by the lowest-energy photons that have not been attenuated, i.e. by photons close to the energy at which the photoelectric absorption optical depth is unity. Significantly higher-energy photons are then less important for this layer.

3 Thomson and Compton scattering

Photoelectric absorption is the dominant interaction of photons with matter for photon energies $\lesssim 10$ keV. For higher energies, Thomson/Compton scattering begins to dominate.

Assume a free free electron (mass m_e, charge e) and a plane electromagnetic wave with wave vector k parallel to $\hat{z}$ and angular frequency ω with $\hbar\omega \ll m_e c^2$. The electron oscillates along x and y

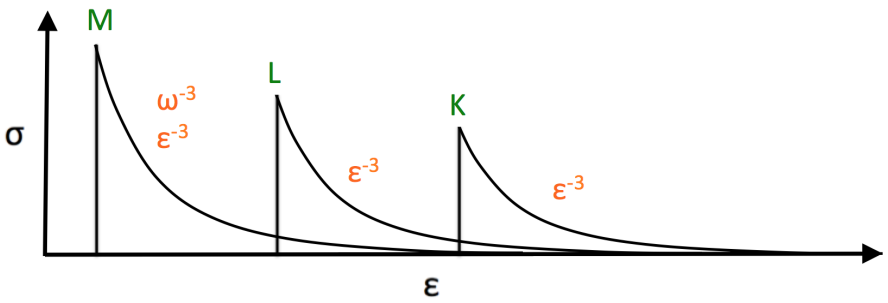

Figure 1. Schematic illustrating the absorption cross sections as a function of photon energy ε (or associated radiation frequency ω) for ionization at the M-, L-, and K shell. Above the ionization threshold, the cross section decreases like ε^{-3} or ω^{-3} (after Shu 1991).

(perpendicular to z) with accelerations of

$$\ddot{x} = -\frac{e\mathcal{E}_x^i}{m_\mathrm{e}}, \qquad \ddot{y} = -\frac{e\mathcal{E}_y^i}{m_\mathrm{e}} \tag{27}$$

where $\mathcal{E}_x^i$ and $\mathcal{E}_y^i$ are the oscillating electric field components of the unpolarized infalling wave with $< \mathcal{E}_x^2 >=< \mathcal{E}_y^2 >$. The indices i and f stand for *initial* (infalling) and *final* (scattered wave).

The oscillating electron emits radiation according to the Larmor formula,

$$dQ(\varphi) = \frac{e^2|\ddot{r}|^2 \sin^2\varphi}{4\pi c^3} d\Omega \quad [\mathrm{erg\ s^{-1}}]. \tag{28}$$

where φ is the angle between the oscillation direction in the xz plane and the outgoing wave vector k^f. Let θ be the scattering angle of a wave in the xz plane (between k^f and the $\hat{z}$ direction). For the electron oscillations along x and y, we find

$$dQ_x \propto |\ddot{x}|^2 \sin^2\varphi, \qquad dQ_y \propto |\ddot{y}|^2. \tag{29}$$

The Poynting vector (energy flux density of the electromagnetic wave) is

$$\mathbf{S} = \frac{c}{4\pi}\mathcal{E}\times\mathbf{B} = \frac{c}{4\pi}|\mathcal{E}|^2\hat{\mathbf{k}}_i \quad [\mathrm{erg\ cm^{-2}s^{-1}}]. \tag{30}$$

The time average of this is

$$S \equiv \langle|\mathbf{S}|\rangle = \frac{2c}{4\pi}\langle\mathcal{E}_x^2\rangle \tag{31}$$

and therefore

$$dQ(\varphi) = \frac{e^4 S_i(\sin^2\varphi+1)}{2{m_\mathrm{e}}^2c^4} d\Omega \quad [\mathrm{erg\ s^{-1}}]. \tag{32}$$

The differential cross section $d\sigma$ is the ratio between the energy flux scattered into $d\Omega$ and the infalling energy flux, S_i,

$$\mathrm{d}\sigma(\varphi) = \frac{dQ}{S} = \frac{e^4 S_i(\sin^2\varphi+1)}{2{m_\mathrm{e}}^2c^4 S_i} d\Omega = \frac{(\sin^2\varphi+1)}{2} a_0^2 d\Omega \equiv \frac{a_0^2}{2}(\cos^2\theta+1)d\Omega \quad [\mathrm{cm^2}], \tag{33}$$

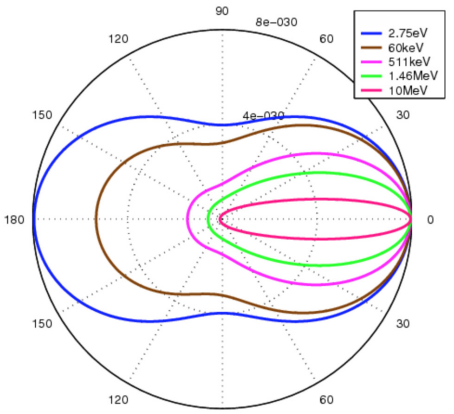

Figure 2. Polar diagram showing the Klein-Nishina scattering cross section for Thomson/Compton scattering for different incoming electron energies (colors). The limiting case for low photon energies (Thomson scattering) is represented by the blue graph. The photon is injected from the left, the electron is initially at rest in the center (from `http://commons.wikimedia.org/wiki/File:Klein-Nishina_distribution.png`).

where $a_0 = e^2/m_e c^2 = 2.8 \cdot 10^{-13}$ cm is the classical electron radius. Integration over $\theta = \pi/2 - \varphi$ gives the total (“Thomson”) scattering cross section,

$$\sigma_T = a_0^2 \int_0^\pi (\sin^2\varphi + 1)\pi \sin\theta \mathrm{d}\theta = \frac{8\pi}{3} a_0^2 \tag{34}$$

and therefore

$$Q = S\sigma_\mathrm{T} \equiv c u_\mathrm{rad} \sigma_\mathrm{T}. \tag{35}$$

Compton scattering is essentially the same process for high photon energies, i.e., $\hbar\omega \gtrsim m_e c^2$ where we need to consider energy and momentum transfer from the wave to the electron, i.e., we need to consider photons. The electron itself will therefore not stay at rest and also propagates at an angle η to the z direction. This case is, however, less relevant for protoplanetary disks irradiated by stellar X-rays. We only provide the relevant Klein-Nishina cross section (ε_i = incoming photon energy, ε_f outgoing photon energy),

$$\mathrm{d}\sigma = \frac{a_0^2}{2}\left(\frac{\varepsilon_i}{\varepsilon_f} + \frac{\varepsilon_f}{\varepsilon_i} - \sin^2\theta\right)\left(\frac{\varepsilon_f}{\varepsilon_i}\right)^2 d\Omega, \qquad \frac{\varepsilon_i}{\varepsilon_f} = 1 + \frac{\varepsilon_i}{m_e c^2}(1 - \cos\theta). \tag{36}$$

Fig. 2 displays a polar diagram showing scattering efficiency as a function of angle, including the low-energy limit for Thomson scattering.

4 Simplified Treatment of Collisional Ionization

Although collisional ionization (e.g., ionization due to an energetic free electron or a cosmic-ray particle) can easily be treated quantum-mechanically, we present here a simple classical approach outlined in Kahn (2005) and going back to Thomson (1912). The quantum-mechanical approach can also be found in Kahn (2005).

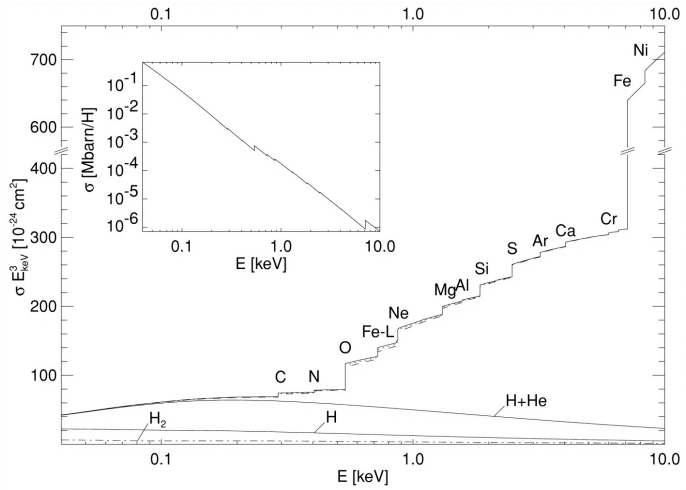

Figure 3. Absorption cross section for a gas with the composition of the interstellar medium, including dust admixture (solid and dotted lines). For the main plot, σ has been multiplied by E^3 for illustration purposes, while the inset shows σ without this multiplier. The contributions of atomic hydrogen, helium, hydrogen plus helium, and molecular hydrogen (H_2) are shown at the bottom of the plot (from Wilms et al. 2000; © AAS. Reproduced with permission).

If two electrons, one being at rest initially (the valence electron in an atom) and the other having kinetic energy E, collide with an impact parameter b, the energy transfer is

$$\Delta E = \frac{E}{1 + \frac{E^2 b^2}{e^4}} \tag{37}$$

For an ionization to happen, ΔE must exceed the ionization potential χ, which implies that the impact parameter must be less than b_c,

$$b_c = \frac{e^2}{E}\left(\frac{E}{\chi} - 1\right)^{1/2} \tag{38}$$

so that the geometric cross section becomes

$$\sigma = b_c^2 \pi = \pi e^4 \frac{1}{E^2}\left(\frac{E}{\chi} - 1\right) \tag{39}$$

where a_2 is the Bohr radius. This expression needs to be summed over all electrons in the atom and their associated χ as long as $E \geq \chi$. The approximation is good as long as $E \gg \chi$.

5 Ionization and Heating by X-Ray Irradiation in Astrophysical Gases

5.1 Energy Partitions and Heating

When X-ray photons with energies above ≈ 600 eV interact with gas, they first ionize predominantly heavy atoms in the inner-shell (K-shell, L-shell; Eq. 26 for hydrogen-like atoms). X-rays below

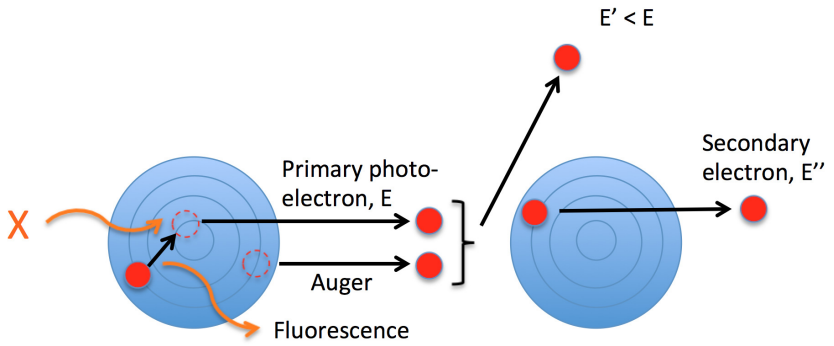

Figure 4. Sketch illustrating primary ionization due to an incoming X-ray (left) and secondary ionization due to photoelectron and Auger electrons (right). Secondary electrons will continue to ionize and excite and also dissociate molecules. Fluorescence as an energy loss path is also shown.

$\approx$ 600 eV predominantly ionize H, H_2, and He. For a pure H_2 gas, the most important reaction is

$$\gamma + H_2 \rightarrow H_2^+ + e. \tag{40}$$

followed by

$$H_2^+ + H_2 \rightarrow H_3^+ + H \tag{41}$$

$$H_3^+ + e \rightarrow H_2 + H \quad \text{or } 3H \tag{42}$$

$$H + H \rightarrow H_2 \quad \text{(on grains)} \tag{43}$$

the first two being exothermic reactions liberating 10.96 eV of which a fraction goes into heat, and the third one liberating 4.5 eV for internal excitation.

The *photoelectron* (Fig. 4) ejected as a consequence of the ionization process carries away the incident photon energy minus the ionization energy, minus $\approx$ 1.1 eV for vibrational excitation (Glassgold & Langer 1973). It is typically an energetic electron (several 100 eV). Furthermore, the inner-shell vacancy in the photoionized atom is filled by an electron from a higher shell. The energy difference may either be radiated away (“fluorescence” emission) or transmitted to another bound, outer electron, thus ejecting it as an *Auger* electron.

Fluorescence is typically important for heavy atoms such a Fe (fluorescent yield = fraction of inner-shell holes filled by emission of a fluorescent photon exceeds 10% for atomic numbers $\gtrsim$ 20 after removal of an 1s electron, see Osterbrock & Ferland 2006). In contrast, lighter elements predominantly eject Auger electrons (that are also produced by heavy atoms). The fluorescent photons themselves are X-ray photons and therefore further continue inducing reactions as listed above.

An *Auger electron* carries away the energy difference between the inner-shell hole and the outer, “valence” shell minus the (small) ionization energy of the valence shell. Because the Kα energy difference is large ($\approx$ 75% of the ionization energy), the Auger electrons can be energetic, of order the binding energy of a K shell electron, $\approx$ 500 eV for neutral O and many keV for neutral Fe (Krolik & Kallman 1983; Osterbrock & Ferland 2006). Neutral Fe and other heavy elements may eject multiple Auger electrons; after creation of a K-shell vacancy, Fe^0 ejects typically six Auger electrons; for higher shells and higher ionization stages, the Auger production decreases (Osterbrock & Ferland 2006).

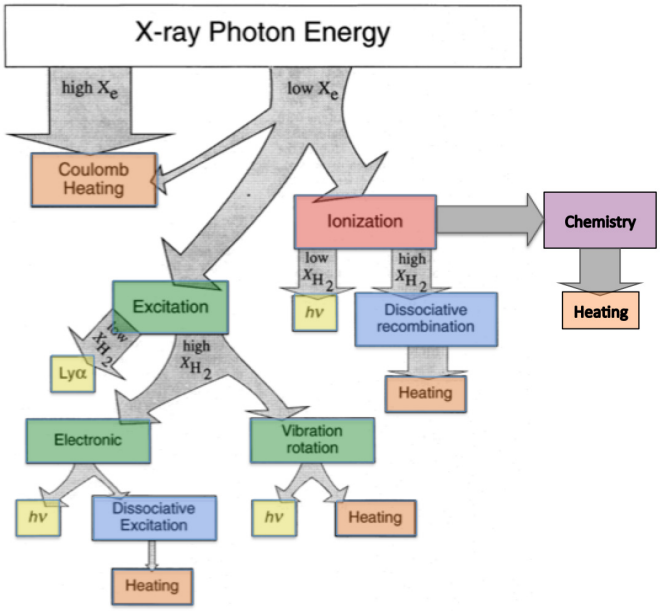

Figure 5. Sketch illustrating the loss channels for an energetic electron injected into a dense gas. The widths of the arrows indicate the approximate fractions of the initial energy channeled into the respective processes (the branching depends on the electron and the H_2 fractions; after Maloney et al. 1996, complemented with the chemical reaction path to the right; © AAS. Reproduced with permission).

Effectively, therefore, almost all of the incident X-ray energy is transferred to energetic electrons (photoelectrons and Auger electrons) that subsequently interact collisionally with other atoms, predominantly H, H_2, and He, thus inducing excitation, dissociation, and secondary ionization at the valence shell (Krolik & Kallman 1983; Lepp & McCray 1983; Weisheit 1974):

$$e + H_2 \rightarrow e + H_2 \quad \text{(elastic scattering)} \tag{44}$$

$$e + H_2 \rightarrow e' + H_2^* \quad \text{(electronic}[E(e) > 11.2\ \text{eV}]\text{/vibrational/rotational excitation)} \tag{45}$$

$$e + H_2 \rightarrow e_1 + e_2 + H_2^+ \quad \text{(ionization for } E(e) > 15.4\ \text{eV)} \tag{46}$$

$$e + H_2 \rightarrow e' + 2H \quad \text{(dissociation for } E(e) > 8.8\ \text{eV)} \tag{47}$$

The ionization channel then leads to further reactions involving H_2^+ as described above, involving heating. Heating is also involved in the dissociation reaction, and in collisional de-excitation of rotational transitions, while de-excitation of electronic and vibrational transitions will lead to photons leaving typical astrophysical systems. For electrons above 10 eV, further ionization, dissociation and electronic excitation are important, while for lower-energy electrons, these channels are essentially irrelevant and the energy mostly ends up in rotational and vibrational excitation and heating through collisions (Shull 1979). Collisional de-excitation of rotational excitations in a sufficiently high-density gas will lead to further heating. This is obviously a basic difference to atomic gas.

For weakly ionized gases, $\approx 40\%$ of the primary electron energy will be used for ionization (Krolik & Kallman 1983; Shull & van Steenberg 1985). The average number of secondary H ionizations

(ground-state binding energy = 13.6 eV) per 1 keV photoelectron is thus 1 keV×0.4/13.6 eV ≈ 30 for atomic hydrogen gas (and ≈ 26 for molecular hydrogen gas, i.e., ≈37 eV are expended for the production of one ion pair). For strongly ionized gases ($n_e/n_{tot} > 0.01$) Coulomb heating dominates (Lepp & McCray 1983; Shull 1979).

The entire chain of ionization, excitation, dissociation and heating reactions (see Fig. 5) has been analyzed in detail for molecular gas by Glassgold & Langer (1973), Dalgarno et al. (1999) and Glassgold et al. (2012). Their results may be summarized as follows, as detailed in Tables 1 and 2 for a H_2 + He neutral gas. Table 1 (after Dalgarno et al. 1999) shows the energy partition for 1 keV of initial electron energy. The columns provide the energy W expended for a given process (W is independent of E as long as $E \gtrsim 200$ eV) although not all energy is required for the primary product of this process; then the number of such processes for E, i.e., $N = E/W$, for $E = 1$ keV; then the threshold energy E_{th} for the process; and finally the energy from this process, i.e., NE_{th}. From the ionization reactions in Table 1, one finds that the average energy used to produce one ion pair (H_2^+, H^+, He^+, and He^{2+}) is 37 eV per keV. 47% of the energy is in ionization, 47% in H_2 and He excitation, and 6% (60 eV per keV) in direct heating and collisional de-excitation of H_2 rotational levels (also heating the gas). Subsequent transformation into heat through chemical reactions, dissociation and collisional de-excitation of these initial products was calculated by Glassgold et al. (2012) and is summarized in Table 2 for an initial 1 keV electron. We note that dissociation of collisionally excited states contributes 57 eV per keV, elastic collisions and collisional de-excitation of rotational states also 57 eV, collisional de-excitation of vibrational levels 141 eV per keV, and chemical heating by reactions between the generated ions and neutrals 252 eV per keV. The total heating thus amounts to 507 eV per keV, or 18.7 eV per produced ion pair, or 51% of the energy expended for the production of an ion pair.

The heating rate can therefore be expressed as

$$\Gamma_X = 4. \times 10^{-11} \zeta_X \left(\frac{\Delta\epsilon_h}{30\ \mathrm{eV}} \right) n_H \quad [\mathrm{erg\ cm^{-3}\ s^{-1}}] \tag{48}$$

(Qi et al. 2006 based on Glassgold et al. 2004), $\Delta\epsilon_h \approx 30$ eV = heating per ionization for H_2 gas.

5.2 Simple Photoionization Estimates in Astrophysical Gases

We provide some rough estimates for ionization in an astrophysical gas irradiated by an point-like X-ray source, following the presentation of Krolik & Kallman (1983). Although a realistic X-ray spectrum can be dominated by lines, especially for soft ($\gtrsim 1$ keV) sources, the details of the spectral energy distribution are less important (see Sect. 5). We approximate the intrinsic source X-ray spectrum by an exponential (appropriate for the bremsstrahlung continuum),

$$F_\varepsilon = F_0 e^{-\varepsilon/kT}, \tag{49}$$

ε being the photon energy and T the source temperature. The radiation suffers photoelectric absorption while entering cold (near-neutral) gas, following the cross section (see Eq. 26)

$$\sigma(\varepsilon) = \sigma_0 \left(\frac{\varepsilon}{kT} \right)^{-3} \tag{50}$$

where the normalization σ_0 is the photoionization cross section at the given kT of the source. Absorption is mainly due to H and He for photons below 600 eV and due to heavier elements above,

Table 1. Energy partitions for 1 keV electrons in neutral gas (H_2, He)

Process	W (eV)	N	$E_{\rm th}$ (eV)	$NE_{\rm th}$ (eV)
H_2^+	41.9	23.87	15.44	369
H^+	921	1.09	18.08	20
He^+	459	2.18	24.59	54
He^{2+}	16000	0.0625	54.52	3
Total ion production		27.2		446
Excitation B	117	8.55	11.37	97
Excitation C	132	7.58	12.42	94
Dissociation	92.6	10.8	~13	140
H+H($2p$)	534	1.87	14.7	28
$v = 1$	7.81	128	0.516	66
$v = 2$	109		1.032	10
Total H_2 excitation		166		435
He 2^1S^e	15000	0.0667	20.62	1
2^1P	1940	0.515	21.22	11
2^3S	34900	0.0287	19.82	1
$2^3P + n > 2^3$	22500	0.0444	21.0	1
$n > 2^1$	3520	0.284	23	7
Total He excitation		0.94		21
Elastic collisions and rotational excitation				57
Grand total		–		959

Table 2. Heating per ion pair and per keV

Process	Q per ion (eV)	Q per keV (eV)
Elastic coll., coll. de-excitation of rotational levels	2.1	57
Dissociation after collisional excitation	2.1	57
Collisional de-excitation of collisionally excited vibrational levels	2.8	76
Collisional de-excitation of vibrational levels excited after fluorescence	2.4	65
Chemical reactions of H_2^+	7.7	209
Chemical reactions of H^+	0.3	8
Chemical/CX reactions of He+	1.3	35
Total heating	18.7	507
Energy for an ion pair	36.8	—

in particular O and, above 7.1 eV, Fe (Wilms et al. 2000, Fig. 3). The primary ionization rate per hydrogen atom is consequently,

$$\zeta_x = \int_{\varepsilon_0}^{\infty} e^{-\tau(\varepsilon)} \frac{F_\varepsilon}{\varepsilon} \sigma(\varepsilon) \mathrm{d}\varepsilon = F_0 \sigma_0 \int_{\varepsilon_0}^{\infty} \frac{1}{x^4} e^{-x-\tau/x^3} \mathrm{d}x \tag{51}$$

where $\tau = \sigma_0 N_{\rm H}$ is the optical depth at the ionization location for photons of energy kT, $N_{\rm H}$ being the equivalent hydrogen column density measured from the source. We have substituted $x \equiv \varepsilon/kT$. Similarly, we obtain for the heating rate per hydrogen atom:

$$G = \int_{\varepsilon_0}^{\infty} e^{-\tau(\varepsilon)} \frac{F_\varepsilon}{\varepsilon} \sigma(\varepsilon) \varepsilon {\rm d}\varepsilon = F_0 \sigma_0 kT \int_{\varepsilon_0}^{\infty} \frac{1}{x^3} e^{-x-\tau/x^3} {\rm d}x \tag{52}$$

Generally, $\varepsilon_0 \gg$ the ionization threshold for H, 13.6 eV.

The structure of an X-ray irradiated gas volume shows a series of nested, distinct regions, starting with a highly ionized "coronal" region close to the source, with temperatures similar to the source temperature ($10^6 - 10^8$ K). It is followed by a H II region at $\sim 10^4$ K determined by the balance between ionization and hydrogen recombination. Next follows, subject to a thermal instability, an atomic H I region at ~8000 K, and then, after a rapid decline in temperature, the molecular H_2 region below 5000 K (Lepp & McCray 1983). Where $T > 700$ K in the H_2 region, vibrational H_2 infrared emission is efficiently produced. Near the dissociation front, H_2 emission is induced by excitation due to thermal collisions, while in cooler regions it follows from a cascade through vibration-rotation states following electronic excitation of H_2 molecules by non-thermal electrons or ultraviolet radiation (Black & Dalgarno 1976; Lepp & McCray 1983).

Krolik & Kallman (1983) perform detailed ionization calculations for molecular gas (in a star-forming region) with a density of $n_{\rm H(atoms)} = 4 \times 10^5$ cm^{-3} and $T = 50$ K. A total of 53 atomic, ionic, and molecular species were linked by 585 chemical reactions. It was assumed that $\approx 45\%$ of the photoelectron and Auger electron energy is effectively used for ionization, the rest going into heating and excitation. The main results of this study demonstrated that the typical ionization rate in a molecular cloud such as the Orion Nebula with embedded T Tauri and hot stars is of the same order of magnitude as the cosmic-ray ionization rate, i.e. $\zeta \approx 10^{-17}$ s^{-1}. Furthermore, given that most of the ionization is due to secondary electrons, the chemistry in the irradiated cloud is similar to the case of cosmic-ray irradiation for similar total ionization rates.

6 Cosmic Rays

6.1 Collisional Ionization by Cosmic Rays

Effects of collisional ionization and heating by cosmic rays (CR) was discussed for *atomic* gas by Spitzer & Tomasko (1968). The CR first ionizes H by ejecting an additional "first-generation secondary electron" with a typical energy of 35-50 eV (Bethe 1933) depending on the CR energy, the more energetic of which produce further ionizations (further "secondaries"). Eventually, the total number of secondaries is 5/3 times the number of first-generation secondaries, and therefore the ionization rate is

$$\zeta_{\rm CR} = \frac{5}{3} \int 4\pi j(E) \sigma_{\rm CR} {\rm d}E \tag{53}$$

where $j(E)$ is the CR spectrum in particles per cm^2 per unit energy per unit solid angle. The observed CR spectrum suggests $\zeta_{\rm CR} \approx 10^{-17}$ s^{-1} in the interstellar medium.

The situation in a molecular environment is more complicated because of the role of vibrational and rotational excitation and dissociation. The primary H_2 ionization event uses 15.4 eV for ionization, 1 eV for vibrational excitation, and on average 19 eV will go into the outgoing electron available for secondary ionization two-thirds of the time (Glassgold et al. 2012). Essentially, the further reactions are the same as those of the electrons liberated by X-ray ionization - see above. The initial CR ionization is in fact comparable to an ionization by the primary electrons in the photoionization case

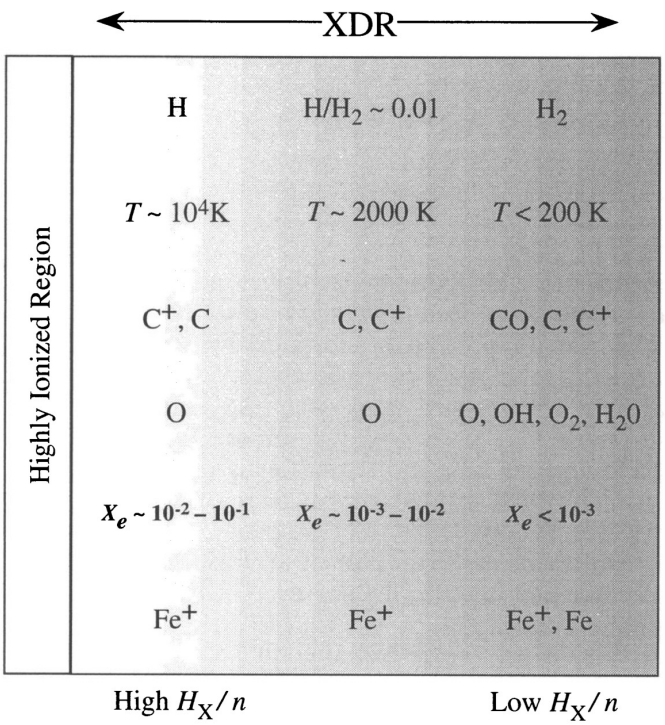

Figure 6. Schematic showing a cut through an X-ray photodissociation region. Approximate temperature, chemical composition, and ionization fractions are given. $H_{\rm X}$ is the energy deposition rate per particle and n is the gas density. The X-rays are injected from the left and are continuously attenuated as they proceed through the medium, the softer photons being absorbed more rapidly (from Maloney et al. 1996; © AAS. Reproduced with permission).

if the *velocities* of the two particle species are the same, i.e., a fast electron behaves similarly as a proton if the electron kinetic energy is $E = (m_{\rm e}/m_{\rm p})E_p$ (Glassgold et al. 2012).

Each secondary electron contributes an average energy E_h to the gas heating. Therefore, the heating rate by cosmic rays can be approximated as (Jonkheid et al. 2004)

$$\Gamma_{\rm CR} = \zeta_{\rm CR}(5.5 \times 10^{-12} n_{\rm H} + 2.5 \times 10^{-11} n_{\rm H_2}) \tag{54}$$

7 Applications to Protoplanetary Disks

Irradiation of protoplanetary disks by X-rays emitted from the hot corona or magnetosphere of the central star is fundamentally important to ionize disks and thereby drive chemical reactions, or the magnetorotational instability and thus accretion. X-rays also heat the upper disk layers and thus induce photoevaporative flows eventually leading to disk dispersal and quenching of planet formation. The importance of stellar X-rays was recognized when X-ray surveys of star-forming regions systematically indicated high X-ray luminosities in T Tauri stars, and partly rather hard spectral energy distributions (Casanova et al. 1995). We discuss ionization, heating and chemical driving separately although all processes occur together and are strongly interlinked, as discussed in the sections above.

7.1 X-Ray and CR Ionization and the Magnetorotational Instability

We follow the same approach as in Eq. 51 approximating the X-ray spectrum by an exponential; however, the stellar X-ray spectrum is continuously being absorbed along the pathway from the star to the disk surface by a disk wind (which is perhaps driven by the X-ray irradiation itself - see below). We follow Glassgold et al. (1997) and separate the dependence of the photon flux spectrum on energy and position (r = radius of the disk segment) for a geometrically thin, flat disk,

$$F_0(\varepsilon, r) = \underbrace{\frac{R}{r}\frac{1}{2}\frac{1}{4\pi r^2}\frac{L_X}{kT}}_{f(r)} \quad \underbrace{\frac{1}{\varepsilon}e^{-\varepsilon/kT}}_{g(\varepsilon)}, \quad \varepsilon > \varepsilon_0 \tag{55}$$

where we have assumed that the X-ray source is located at the center of the disk but vertically displaced by $R \ll r$; R/r thus is the glancing angle at which the X-rays strike the disk; the $1/\varepsilon$ factor transforms energy flux to photon flux; the $1/(kT)$ factor normalizes the total luminosity to L_X, and ε_0 is introduced to simulate the low-energy cutoff due to absorption along the way from the star to the disk.

On encountering the disk gas, the X-rays are continuously being attenuated by photoelectric absorption, i.e. the total ionization rate is calculated from (see Eq. 51)

$$\sigma(\varepsilon) = \sum_k x_k \sigma_k(\varepsilon) = \text{total photoionization cross section per H nucleus} \tag{56}$$

$$\tau(r, \varepsilon) = \frac{r}{R} N_\perp(r)\sigma(\varepsilon) = \text{optical depth for X} - \text{rays with energy } \varepsilon \tag{57}$$

$$\zeta_X = f(r) \sum_k \int_{\varepsilon_k}^{\infty} g(\varepsilon) e^{-\tau(\varepsilon)} \sigma_k(\varepsilon) \left(\frac{\varepsilon - \varepsilon_k + \epsilon_k}{\Delta\varepsilon} \right) \mathrm{d}\varepsilon \tag{58}$$

where here we have summed over all elements k with abundance x_k, photoionization cross section σ_k (rather than assuming $\sigma(\varepsilon) \propto \varepsilon^{-3}$ as adopted in Eq. 51), ionization potential ε_k, and average Auger energy ϵ_k (assumed to be = ε_k in Eq. 51). $\Delta\varepsilon \approx 37$ eV is the average energy needed for a collisional ionization of H or H_2, and $N_\perp$ is the vertical hydrogen column density into the disk. Eq. 58 shows that, if Auger $\epsilon_k \approx \varepsilon_k$ (ionization energy), essentially all of the initial X-ray energy ε is used up to produce ionization, expending $\Delta\varepsilon \approx 37$ eV per ionization pair. For photon energy ε, integration is over the cross section σ_k starting at the ionization edge ε_k for the considered species k. The sum is over all possible species.

Numerical evaluation of these expressions for a realistic disk profile were performed by Glassgold et al. (1997); Igea & Glassgold (1999) improved these calculations for more realistic disk shapes and consideration of Compton scattering of energetic X-rays. The results can be summarized as follows (see Fig. 7):

- the ionization rate by the softest X-rays at the disk surface at optical depth $\ll 1$ is approximately constant, owing to the spectral cutoff ε_0;
- the ionization rate rapidly decreases toward larger column depths where harder photons of the spectrum ionize predominantly heavier elements;
- harder spectra penetrate deeper into the disk and therefore ionize deeper layers;
- for a typical stellar coronal temperature of $kT = 1$ keV, the ionization degree corresponding to the adopted cosmic-ray ionization degree of 2×10^{-17} s^{-1} is found at depths of $N_H \approx 10^{23-25}$ cm^{-2} at disk radii of $\approx 10 - 1$ AU.

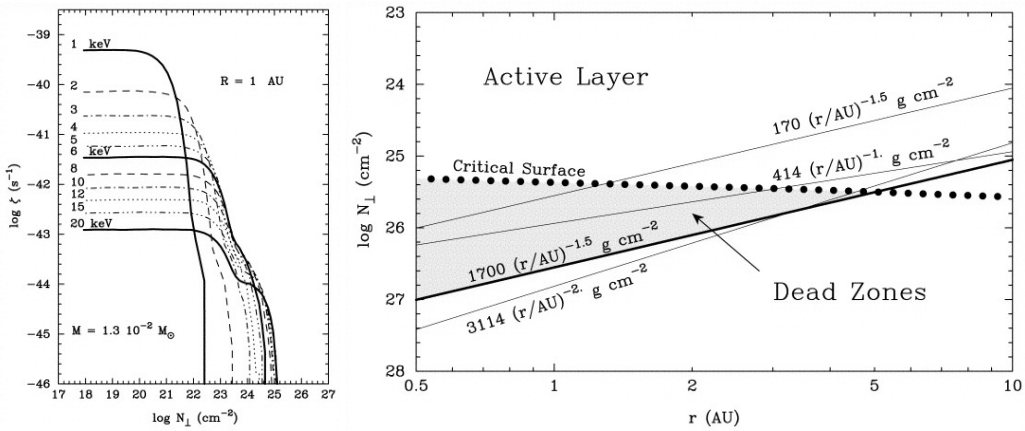

Figure 7. *Left:* Ionization rates for monochromatic X-rays as a function of column density vertically into a disk for a gas with standard interstellar composition, at a radius of 1 AU. The source X-ray luminosity has been normalized to 1 erg s^{-1}. The shoulder at deep levels are due to Compton scattering (from Igea & Glassgold 1999). – *Right:* Electron fraction in a disk due to X-ray ionization, shown in the radius - $N_\perp$ (vertical column density) plane. "Critical surface" marks the height below which the ionization fraction is too low to induce the magnetorotational instability. The solid lines give disk mid-planes from different models (from Igea & Glassgold 1999; © AAS. Reproduced with permission).

- At column densities greater than $N_{\rm H} \approx 1.5 \times 10^{24}$ $\rm cm^{-2}$, the ionizing X-rays have energies > 10 keV where the Compton cross section becomes larger than the absorption cross section, and ζ_X begins to be altered by Compton scattering.

The ionization fraction follows from the balance between ζ_X and the dissociative recombination rate with molecular ions. Consider a simple model (Oppenheimer & Dalgarno 1974) involving molecules $\rm m_j$ and a heavy atoms $\rm M_i$, their ions $\rm m_j^+$ and $\rm M_i^+$, and free electrons e. Densities of these species are denoted by $n(...)$, and n is the total particle density, $n(\rm m) = \sum_j n(m_j)$, $n(\rm M) = \sum_i n(M_i)$ and analogous for the ions $\rm m^+$ and $\rm M^+$. The adopted "chemical reactions" are

Ionization of all $\rm m_j$	$\rm m_j \rightarrow m_j^+ + e$	total rate ζ_X
Dissociative recombination of molecule $\rm m_j$	$\rm m_j^+ + e \rightarrow m_j$	rate coeff. α_j
Radiative recombination of atom $\rm M_i$	$\rm M_i^+ + e \rightarrow M_i + h\nu$	rate coeff. γ_i
Charge exchange between $\rm m_j$ and $\rm M_i$	$\rm M_i + m_j^+ \rightarrow M_i^+ + m_j$	rate coeff. β_{ji}

The following relations apply to this simple system:

$$\text{Electron density} \qquad n(\rm e) = \sum_i n(M_i^+) + \sum_j n(m_j^+) \tag{59}$$

$$\text{Variation of } n(\rm e) \qquad \frac{{\rm d}n(\rm e)}{{\rm d}t} = \zeta_X n - \sum_j \alpha_j n(m_j^+) n(\rm e) - \sum_i \gamma_i n(M_i^+) n(\rm e) \tag{60}$$

$$\text{Variation of } n(\rm m_j^+) \qquad \frac{{\rm d}n(m_j^+)}{{\rm d}t} = f_j \zeta_X n - \alpha_j n(m_j^+) n(\rm e) - \beta_{ji} n(M_i) n(m_j^+) \tag{61}$$

where f_j is the fraction of ionizations creating the molecular ion m_j^+. Using the equilibrium condition $\mathrm{d}/\mathrm{d}t = 0$ and adopting, for a simplifying approximation, $\alpha_j = \alpha, \beta_{ji} = \beta, \gamma_i = \gamma$ independent of i and j, one finds (Oppenheimer & Dalgarno 1974)

$$n(\mathrm{e})^3 + \frac{\beta n(\mathrm{M})}{\alpha} n(\mathrm{e})^2 - \frac{\zeta_X n}{\alpha} n(\mathrm{e}) - \frac{\zeta_X n \beta n(\mathrm{M})}{\alpha\gamma} = 0 \tag{62}$$

Typically, $\alpha \gg \gamma$. Various assumptions can be made to solve this equation for $n(\mathrm{e})$. For a purely molecular gas, we may neglect terms with M and keep only the first and the third term, from which we find for the electron fraction $x_\mathrm{e} = n_\mathrm{e}/n$

$$x_\mathrm{e} = \left(\frac{\zeta_X}{n\alpha}\right)^{1/2} \tag{63}$$

where, in a realistic situation for protoplanetary disks, $\alpha \approx 2 \times 10^{-6} T^{-1/2}$ cm^3 s^{-1} and n is the hydrogen number density (Glassgold et al. 1997; Igea & Glassgold 1999). Calculations by Glassgold et al. (1997) and Igea & Glassgold (1999) show (accounting for sedimentation of condensible heavy elements) that $n(\mathrm{e})$ decreases rapidly toward the disk midplane; for a given vertical column density $N_\perp$, $n(\mathrm{e})$ decreases with distance r; together, the disk ionization structure is stratified in such a way that a given ionization fraction defines a wedge-shaped region around the inner disk mid-plane with its apex at the mid-plane at some outer radius (Fig. 7b).

The magnetorotational instability (Balbus & Hawley 1991) requires a minimum ionization degree for magnetic fields to couple to the disk gas and maintain magnetic turbulence; this process is held responsible for disk accretion. Disk regions that fulfill the ionization criterion for the instability are "active", other regions are referred to as "dead zones" (Gammie 1996). The criterion is actually given by the magnetic Reynolds number, Re_M. From Ampère's, Faraday's and Ohm's equations, one finds the *induction equation*

$$\frac{\partial \mathbf{B}}{\partial t} = \nabla \times (v \times \mathbf{B}) + \eta \nabla^2 \mathbf{B} \tag{64}$$

where $\eta \equiv c^2/(4\pi\sigma)$ is the magnetic diffusivity, with σ being the electric conductivity, and v is the plasma flow velocity. The magnetic Reynolds number expresses the relative importance between advection (the first term on the RHS) and magnetic diffusion (the second term),

$$Re_\mathrm{M} = \frac{Lv}{\eta} \approx 7.4 \times 10^{13} x_\mathrm{e} \alpha^{1/2} \left(\frac{R}{1\ \mathrm{AU}}\right)^{3/2} \left(\frac{T}{500\ \mathrm{K}}\right) \left(\frac{M}{M_\odot}\right)^{-1/2} \tag{65}$$

where L is the characteristic length of variations in B, and the last numerical expression is due to Gammie (1996), with α being the Shakura-Sunyaev viscosity parameter ($\alpha^{1/2}$ is of order unity). For MRI to be efficient, the critical Re_M is about 100, and this corresponds to an ionization fraction of $\approx 10^{-12}$ (see discussion in Fromang et al. 2002).

Computing the loci of the critical ionization fraction for the operation of the magnetorotational instability (Balbus & Hawley 1991), Glassgold et al. (1997) and Igea & Glassgold (1999) find that a significant part of the disk surface will couple sufficiently to magnetic fields to drive the instability, while the central layer around the midplane of the inner (few AU) disk is insufficiently ionized and is therefore not subject to the instability ("dead zone" not participating in MRI-driven accretion; Fig. 7b; see Turner et al. 2014 for a discussion of non-ideal MHD effects working against MRI).

More detailed considerations of small amounts of metallic atomic may be needed, however. Fromang et al. (2002) find for a standard molecular α disk and $Re_\mathrm{M,crit} = 100$ a dead zone extending from a fraction of an AU out to 10–100 AU. However, a small admixture of heavy-metal atoms is

rapidly ionized by charge exchange with the molecular ions, but atomic ions recombine only slowly by radiation. For standard disks, an atomic abundance of heavy metals of as little as $10^{-6} - 10^{-7}$ of the cosmic value may make the entire disk active, without any dead zone. Newer calculations including complex chemical networks, however, show the presence of a dead zone even if metals are present (Walsh et al. 2012, Cleeves et al. 2013).

In a somewhat complementary approach, the work by Gorti & Hollenbach (2004) addresses mostly the disk *midplane* of evolved ("transitional") disks with low gas and dust densities and inner holes. These disks are optically thin ($\tau_V \lesssim 5$) in the continuum although gas lines may be optically thick. Chemistry includes a simple network for 73 species (atoms, ions, molecules, and molecular ions) with ion-neutral, neutral-neutral, and photoionization reactions, amounting to 537 reactions in total. Ionization and photodissociation lead to local heating of the gas and drive the chemistry. X-rays dominate in heating of the *mid-plane* in the innermost disk, but also the disk surface layers at AU distances. Most of the heat energy is carried away by dust emission and the [O I] 63μm line which is in fact predicted to *strongly correlate with the X-ray irradiation level.* The entire chemistry in the inner disk and on the disk surface layer of this model is found to be *dominated by photoionization and photodissociation caused by UV and X-rays.*

Cosmic rays are efficient in ionizing disk material. Their importance for driving MRI was recognized in particular by Gammie (1996) who developed a model of layered accretion in T Tauri disks. The crucial question is that of the ionization rate. In the interstellar space, $\zeta_{\rm CR} \approx 10^{-17}$ s^{-1} (Spitzer & Tomasko 1968). Gammie (1996) used a limit for the magnetic Reynolds number of $Re_{\rm M} \gtrsim 1$ for the operation of MRI, and adopted the interstellar ionization rate. Using the equilibrium condition Eq. 63 between ionization and (gas-phase) dissociative recombination, he showed that, for typical disk parameters (e.g., $n_{\rm H} \approx 10^{13}$ cm^{-3}) the criterion for instability is marginally fulfilled in the top layers of the disk. However, larger $Re_{\rm M} \approx 100$ may be required (see Fromang et al. 2002).

Another significant problem is the propagation of cosmic rays onto the disk surface. In the present solar system, low-energy cosmic rays are suppressed because of diffusion, convection and adiabatic cooling in the solar wind. The low-energy cosmic-ray spectrum is therefore highly uncertain for energies $\lesssim 10^9$ eV due to modulation of the interstellar CR spectrum by the magnetized solar wind (filling the "heliosphere"). Various extrapolations down to lower energies provide largely diverging spectra (see summary by Cleeves et al. 2013). The interstellar ionization rate is therefore unlikely to be appropriate for a protoplanetary disk environment, especially because T Tauri stars are, like the Sun, producing magnetic fields and are very likely to produce ionized winds. Cleeves et al. (2013) estimate the ionization rate expected for a protoplanetary disk from estimates of the much enhanced magnetic activity of a T Tauri star compared to the present-day Sun, using knowledge of the CR modulation during the solar activity cycle. They conclude that an enhanced T Tauri heliosphere attenuates the cosmic ray flux at, say, 1 AU from the star by ≈3 orders of magnitude compared to the Sun and at least 6 orders of magnitude compared to interstellar conditions. The total CR ionization rate is therefore estimated to be at levels of $\zeta_{\rm CR} \approx 10^{-22} - 10^{-20}$ s^{-1}. In the disk midplane, radioactive decay will provide a floor to the ionization rate, and higher layers of the disk will be ionized predominantly by stellar X-rays. The CR exclusion by T Tauri winds therefore results in much larger "dead zones" in protoplanetary disks, possibly reaching out to distances of 25 AU.

7.2 X-Ray Heating and Photoevaporation

X-rays heat, in conjunction with ionization, the upper layers of protoplanetary disks substantially. In their pioneering work a decade ago, Glassgold et al. (2004) modeled disk heating by stellar X-rays in conjunction with heating by viscous accretion and by stellar winds, based on a thermo-chemical disk

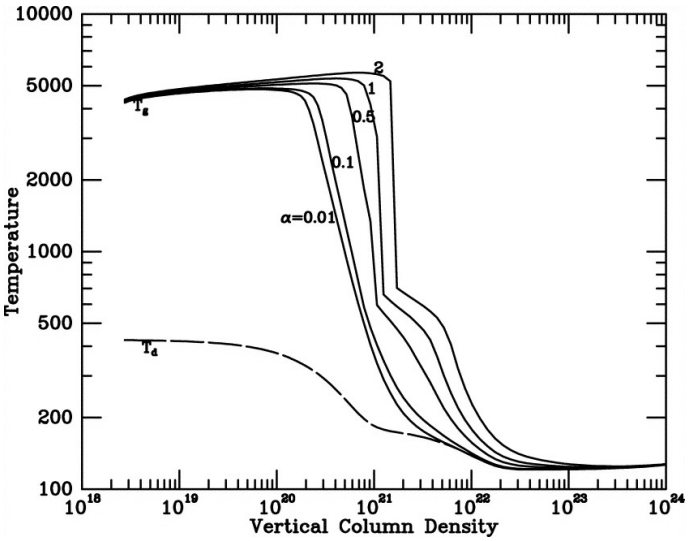

Figure 8. Gas and dust temperature profiles as a function of vertical column density into a disk, at 1 AU from a central T Tauri star; apart from X-ray heating, viscous heating is present, characterized by the various α values ($\alpha = 0$ for no viscous heating; from Glassgold et al. 2004; © AAS. Reproduced with permission).

model. The heating rate due to X-rays can be expressed in terms of the ionization rate (see Eq. 48)

$$\Gamma_X = \zeta_X \Delta\epsilon_h n_{\rm H} \tag{66}$$

where $\Delta\epsilon_h$ simply defines the heating rate per ionization. There are two components to consider, direct X-ray heating $\Delta\epsilon_{h1} \approx 10$ eV per ionization and indirect heating $\Delta\epsilon_{h2} \approx 20$ eV per ionization owing to the increase in X-ray produced electronically excited states that heat gas by collisional de-excitation. Therefore, $\Delta\epsilon_h \approx 30$ eV.

These calculations show that the upper, *atomic* layers of the disk are heated by X-rays (and/or viscous dissipation) to several thousand K at 1 AU (for typical stellar X-ray luminosities; Fig. 8). A strong temperature inversion is thus seen along the vertical direction through the disk. At $N_\perp \approx 10^{21}$ cm^{-2}, the temperature steeply drops and eventually approaches the dust temperature which remains much lower even in the upper layers of the disk. X-ray heating is most efficient in the range of $N_\perp = 10^{19} - 10^{22}$ cm^{-2}. The heating rate increases from the top down because of the increasing hydrogen density, but then declines again because of progressive X-ray attenuation. Monte-Carlo simulations by Ercolano et al. (2008) support this picture, but also show much hotter “disk coronae” closer to the star, which eventually become fully ionized at temperatures up to $\approx 10^6$ K at a fraction of an AU. X-rays are very important heating agents (for standard stellar and disk parameters) out to $\sim 35 - 40$ AU but disk ionization by stellar X-rays can be seen out to 190 AU in these models.

In the transition region where T drops rapidly, at $N_\perp \approx (1 - 2) \times 10^{21}$ cm^{-2}, CO cooling is important. In fact, CO is formed there where H still abounds in its atomic form, and accelerates cooling through CO ro-vibrational and CO rotational emission, generating a strong temperature gradient; corresponding emission lines provide important observational diagnostics of disk heating.

The temperature of the disk “surface” may eventually reach temperatures at which individual particles can leave the system. This occurs once the mean particle energy, $\sim kT$, exceeds the gravitational

binding energy of the particles with mass m, GM_*m/R. For a given temperature, this process of *photoevaporation* becomes effective beyond the *gravitational radius*, R_g, where the above criterion is fulfilled, i.e.,

$$R_g = \frac{GM_*}{c_s^2} \tag{67}$$

where $c_s = (kT/m)^{1/2}$ is the sound speed of the ionized gas. Obviously, then, external heating can be an efficient agent to drive disk dispersal.

There are three important observational boundary conditions to consider for photoevaporation. The first is the actual mass loss attributed to a disk wind, very likely to be identified with photoevaporation. Apart from the often observed fast (≈ 300 km s^{-1}) jets, low-velocity winds (a few to a few tens of km s^{-1}) are seen in many T Tauri spectra, indicating mass loss rates of order $10^{-10} - 10^{-8}$ $M_\odot$ yr^{-1} (Hartigan et al. 1995). The other two boundary conditions relate to time scales. Statistically, protoplanetary dust disks as seen in the infrared disperse with a time scale of $\approx$3 Myr (Mamajek 2009). However, the actual removal of an optically thick disk occurs rapidly at the end of this process, on a time scale of perhaps 0.5 Myr. This "two-time scale problem" has initially been addressed for EUV irradiation of protoplanetary disks. The "UV switch" model by Clarke et al. (2001) assumes that the mass accretion rate initially largely exceeds the wind evaporation rate, so that the disk evolves on an accretion time scale. However, at some point the accretion rate falls below the wind mass loss rate at a certain radius of the disk, at which point the resupply of the inner disk is suppressed and a gap is forming at this distance. The inner disk now disperses on its own, short time scale.

The EUV photoevaporation model of disks was first and extensively developed by Hollenbach et al. (1994). Because a typical disk is optically thick to Ly continuum radiation, it is rather the diffuse recombination radiation field that ionizes the disk gas at large radii. From such models, Hollenbach et al. (1994) derived an expression for the mass-loss rate that depends on the flux of EUV photons, Φ, and the mass of the central star, M_*,

$$\dot{M}_w \approx 4.4 \times 10^{-10} \left(\frac{\Phi}{10^{41}\ \mathrm{s}^{-1}}\right)^{1/2} \left(\frac{M_*}{1 M_\odot}\right)^{1/2} M_\odot\ \mathrm{yr}^{-1}. \tag{68}$$

These models assume that the disk mass above a height where the escape criterion is fulfilled flows away at sound speed of the ionized gas, $c_s \approx 10$ km s^{-1}, so that the mass loss rate per unit disk surface area is ρc_s and the total mass loss rate at radius R is

$$\dot{\Sigma}_w(R) = 2\mu m_\mathrm{H} n_0(R) c_s(R) \tag{69}$$

where μ is the mean molecular weight of the gas ($\approx$ 2.3 for a molecular gas), m_H is the mass of a hydrogen atom, the factor of 2 accounts for the two sides of the disk, and n_0 is the number density of the disk gas.

However, once the inner disk has drained, there is a significant contribution of *direct* radiation supporting the evaporation process in particular at the inner edge of the disk so that the outer disk also rapidly disperses. Such models have been studied in detail and extended by Alexander et al. (2006a). They find that the escape speed is typically $0.4c_s$ and derive a mass-loss formula,

$$\dot{M}_w(< R_\mathrm{out}) \approx 2.2 \times 10^{-9} \left(\frac{\Phi}{10^{41}\ \mathrm{s}^{-1}}\right)^{1/2} \left(\frac{R_\mathrm{in}}{3\ \mathrm{AU}}\right)^{1/2} \left(\frac{H/R}{0.05}\right)^{-1/2} \left[1 - \left(\frac{R_\mathrm{in}}{R_\mathrm{out}}\right)^{0.42}\right] M_\odot\ \mathrm{yr}^{-1} \tag{70}$$

where R_in and R_out are the inner and outer disk radii, respectively, and H/R is the ratio (assumed to be constant) between disk scale height H and radius R. The effect of direct radiation thus enhances the

mass loss rate by an order of magnitude above the estimate in Eq. 68. Numerical simulations confirm this behavior and suggest that at the end of the disk lifetime (several Myr), the disk rapidly disperses within $\gtrsim 10^5$ yr (Alexander et al. 2006b).

EUV (Ly continuum) radiation is problematic because it may not reach the disk at all if disk winds absorb them early on. EUV may therefore be more important at late disk evolution stages (Gorti & Hollenbach 2009) although Pascucci et al. (2014) claim that the EUV contribution is, based on observational evidence, too small to be effective for photoevaporation. An extension to X-rays seems in order. There are significant changes to the picture, however. Apart from the complex ionization and heating theory described further above that is now required, the indirect, diffuse field is unimportant for X-rays. X-rays mostly propagate along the radial direction and deposit heat at the place of their photoabsorption. Initial estimates of mass loss driven by X-ray heating indicated mass loss rates at best comparable to EUV-driven mass loss rates, and probably much lower (Alexander et al. 2004). More recent models based on Monte-Carlo methods for radiation exhibit, however, mass loss rates about one order of magnitude higher, thus perhaps dominating mass-loss by high-energy (ionizing) photons, with wind mass-loss rates of order 10^{-8} $M_\odot$ yr^{-1} (Ercolano et al. 2008). The important advantage of X-rays here is their much larger penetration depths than for EUV, resulting in a much larger disk area subject to photoevaporation (out to $\sim$ 40 AU) compared to the EUV case (for which the inner cutoff at $R_g \approx 5$ AU for 10^4 K gas limits the evaporation efficiency additionally).

The latter studies find that the soft X-ray regime is the most efficient for photoevaporation. While EUV is subject to too much absorption along the paths between star and disk, harder X-rays penetrate too deeply into the disk where they deposit their energy into a larger volume, thus not contributing much to the disk surface heating (Ercolano et al. 2009). These studies were qualitatively and quantitatively supported by full hydrodynamic simulations by Owen et al. (2010) and Owen et al. (2011), emphasizing that the soft X-ray part of a stellar spectrum is the dominant driving mechanism for photoevaporation (rather than EUV alone). Their initial model, using a standard disk and a star with $L_X = 2 \times 10^{30}$ erg s^{-1}, produces photoevaporation in a large range of radii, from 1–70 AU, with a mass-loss rate of about 1.4×10^{-8} $M_\odot$ yr^{-1}. A hole develops first around 1 AU. Furthermore, they find the mass-loss rate to scale linearly with L_X.

Observationally, photoevaporative flows have been reported recently in particular from observations of slightly blueshifted mid infrared lines of Ne II, but may equally be related to observations of “slow winds” seen in O I 6300 Å lines (Hartigan et al. 1995). Analysis of Ne II lines is particularly important since it relates directly to the uppermost material in a disk that has been ionized by the same X-ray radiation. Blueshifts of order a few km s^{-1} are seen in some T Tauri stars (Herczeg et al. 2007; Najita et al. 2009; Pascucci et al. 2007; Pascucci & Sterzik 2009) but caution is in order because a mixture of photoevaporative winds, contributions from fast jets, and emission from steady disk surfaces may be present (Baldovin-Saavedra et al. 2011).

7.3 X-Ray Driven Disk Chemistry

Ultraviolet and X-ray irradiation of astrophysical gases drives chemical reactions in, respectively, photon dominated regions (PDRs) at the surfaces of clouds and in X-ray dominated regions in deeper volumes in the clouds, given their deep penetration depths. Detailed models and comparisons between PDRs and XDRs including ionization, excitation, heating, cooling, and results from advanced chemical networks were computed by Meijerink & Spaans (2005).

Given the importance of X-rays and cosmic rays in ionizing and heating disk gas and the importance of ion chemistry, the interest in X-ray driven chemistry in disks is evident. This lets us enter immediately in the complications of chemical networks, but we circumvent a deeper discussion on such models here in favor of two issues: i) reactions of specific interest directly induced by X-rays,

in particular those illustrating some principal destruction routes of molecular ions; and ii) some key model results based on comprehensive thermo-chemical approaches to disk modeling.

Among the principal ion destruction paths are the following, leading to "chemical heating (Glassgold et al. 2012, see Sect. 5.1):

$H_2^+ + e \rightarrow H + H$
$H_2^+ + H_2 \rightarrow H_3^+ + H$
$H_3^+ + e \rightarrow H_2 + H$
$H_3^+ + e \rightarrow H + H + H$
$H_3^+ + CO \rightarrow HCO^+ + H_2$
$H_3^+ + O \rightarrow OH^+ + H_2$
$H_3^+ + H_2O \rightarrow H_3O^+ + H$
$HCO^+ + e \rightarrow CO + H$
$OH^+ + H_2 \rightarrow H_3O^+$
$H_3O^+ + e \rightarrow H_2O + H$
$H_3O^+ + e \rightarrow OH + H_2$
$H_3O^+ + e \rightarrow OH + 2H$
$H^+ + H_2O \rightarrow H_2O^+ + H$
$H_2O^+ + H_2 \rightarrow H_3O^+ + H$
$He^+ + CO \rightarrow C^+ + O + He$
$C^+ + H_2O \rightarrow HCO^+ + H$

Complex thermo-chemical models of irradiated disks show that the abundances of neutral molecules such as CO, OH, and H_2O are not overly sensitive to X-ray irradiation (a change by less than an order of magnitude over the range of many orders of magnitude in L_X). In contrast, the X-ray sensitive ionization fraction in the upper layers of the disk strongly influences ion chemistry. The following reactions are important (Aresu et al. 2011):

$H_2 + e \rightarrow H_2^+$
$H_2^+ + H_2 \rightarrow H_3^+$
$H_3^+ + O \rightarrow OH^+$ OH^+ grows approximately linearly with L_X.
$H_3^+ + OH \rightarrow H_2O^+$ H_2O^+ grows somewhat less than OH^+.
$H_3^+ + H_2O \rightarrow H_3O^+$ H_2O^+ grows by factor of 10-100 over a factor of 1000 in L_X.
N^+ reacts very sensitively to the presence of X-rays and grows about linearly with L_X.

These reactions also spread in disk area, being pushed to larger distances as L_X grows. A special case of interest is the fine-structure emission of [O I]. The models clearly predict a linear growth of its line flux with the sum of $L_X + L_{UV}$. Whichever of the two luminosities dominates determines the correlation. Because of the usually appreciable UV field around T Tauri stars, an X-ray dependence comes into play only above $L_X \approx 10^{30}$ erg s^{-1} (Aresu et al. 2014). Observations support the flux levels approximately although the correlation is not evident, possibly due to some influence by other parameters such as grain size distribution, surface density distribution, etc. in real objects.

The complexity of chemical networks and the correspondingly expensive computing time of advanced models motivated researchers to study reduced networks that represent the dominant chemical networks, but then allow to study disk structure and evolution more comprehensively. Semenov et al. (2004) utilized a detailed disk model irradiated by a stellar X-ray and UV source and cosmic rays, and furthermore subject to radioactive decay; three distinct layers of the disk were analyzed: the midplane ionized by cosmic rays and radionuclids requiring a reduced network of only 10 species and a similar number of reactions; the intermediate layer ionized by stellar X-rays requiring more complex chemistry between more than 100 species with hundreds of reactions; and the surface layer subject to a set of photoionization-recombination processes, using 21 species and 27 reactions.

8 Irradiating EUV/X-Ray Sources

This section provides a short summary of X-ray sources relevant for irradiation, ionization, and heating of protoplanetary disks.

8.1 Stellar X-Rays

As judged from the temperature structure, flaring behavior, or rotational modulation, X-ray emission from TTS mostly originates from magnetic coronae, with characteristics comparable to more evolved

active main-sequence stars. X-rays from CTTS saturate at a level of $\log(L_X/L_{bol}) \approx -3.5$ (Telleschi et al. 2007). Note that for the Sun, $L_X \approx 2 \times 10^{27}$ erg s^{-1} and $L_{bol} \approx 3.85 \times 10^{33}$ erg s^{-1}. Flaring is common in TTS (Stelzer et al. 2007), the most energetic examples reaching temperatures of $\approx 10^8$ K (Imanishi et al. 2001).

Class I protostars have amply been detected in X-rays by XMM-Newton and Chandra although sample statistics are biased by the X-ray attenuation, favoring detection of the most luminous and the hardest sources. Overall, X-ray characteristics are very similar to T Tauri stars, confirming that magnetic coronae are present at these earlier stages. In the Orion region, the X-ray luminosities increase from protostars to TTS by about an order of magnitude, although the situation is unknown below 1–2 keV (Prisinzano et al. 2008). No significant trend is found for the electron temperatures, which are similarly high (≈1–3 keV) for all detected classes.

8.2 Stellar X-Ray Flares

A flare is a manifestation of a sudden release of magnetic energy in the solar or in a stellar corona. Observationally, flares reveal themselves across the electromagnetic spectrum, usually showing a relatively rapid (minutes to hours) increase of radiation up to the "flare peak" that may occur at somewhat different times in different wavelength bands, followed by a more gradual decay (lasting up to several hours).

Increased temperatures during flares are a consequence of efficient heating mechanisms. Spectral observations of large stellar flares have consistently shown electron temperatures up to 100 MK, in some cases even more (e.g., Tsuboi et al. 1998). Somewhat unexpectedly, the flare peak temperature, T_p, correlates with the peak emission measure, EM_p (or, by implication, the peak X-ray luminosity), roughly as

$$EM_p \propto T_p^{4.30\pm0.35} \tag{71}$$

(Güdel 2004) although observational bias may influence the precise power-law index.

8.3 X-Ray Fluorescence

Photoionization of cool material by X-ray photons above the Fe K edge at 7.11 keV produces a prominent line feature at 6.4 keV (Fe Kα feature). This feature is usually too faint to be detected in any stellar X-ray spectrum; but exceptions include a few T Tauri stars for which fluorescence on the circumstellar disk due to irradiation by stellar X-rays has been proposed.

A meaningful sample of CTTS fluorescent signatures is available (Tsujimoto et al. 2005), with several unexpected features deserving further study. Specifically, strong fluorescence in the Class I protostar Elias 29 (in the ρ Oph region) appears to be quasi-steady rather than related to strong X-ray flares (Favata et al. 2005); even more perplexing, the 6.4 keV line is modulated on time scales of days regardless of the nearly constant stellar X-ray emission; it also does not react to the occurrence of appreciable X-ray flares in the light curve (Giardino et al. 2007). The latter authors suggested that here we see 6.4 keV emission due to non-thermal electron impact in relatively dense, accreting magnetic loops.

8.4 Accretion-Induced X-Rays

Accretion streams falling from circumstellar disks toward the central stars reach a maximum velocity corresponding to the free-fall velocity,

$$v_{ff} = \left(\frac{2GM_*}{R}\right)^{1/2} \approx 620 \left(\frac{M}{M_\odot}\right)^{1/2} \left(\frac{R}{R_\odot}\right)^{-1/2} \left[\text{km s}^{-1}\right]. \tag{72}$$

This velocity is an upper limit as the material starts only at the inner border of the circumstellar disk, probably following curved magnetic field lines down toward the star; a more realistic terminal speed is $v_\mathrm{m} \approx 0.8 v_\mathrm{ff}$ (Calvet & Gullbring 1998). Upon braking at the stellar surface, a shock develops which, according to the strong-shock theory, reaches a temperature of

$$T_\mathrm{s} = \frac{3}{16k} m_\mathrm{p} \mu v_\mathrm{m}^2 \approx 3.5 \times 10^6 \frac{M}{M_\odot} \left(\frac{R}{R_\odot} \right)^{-1} \quad [\mathrm{K}] \tag{73}$$

(where m_p is the proton mass and μ is the mean molecular weight, i.e., $\mu \approx 0.62$ for ionized gas). For typical T Tauri stars, $M = (0.1 - 1) M_\odot$, $R = (0.5 - 2) R_\odot$, and $M/R \approx (0.1 - 1) M_\odot / R_\odot$ and therefore $T_\mathrm{s} \approx (0.4 - 4) \times 10^6$ MK. Such electron temperatures should therefore produce soft X-ray radiation. The bulk of the ensuing X-rays are probably absorbed in the shock, contributing to its heating, although part of the X-rays may escape and heat the pre-shock gas (Calvet & Gullbring 1998); suggestive evidence for accretion-related X-ray production is available in the very soft X-ray range (e.g., based on flux excess in the O VII and Ne IX line triplets or indications of very high densities; Güdel & Telleschi 2007; Kastner et al. 2002).

8.5 Jets and Herbig-Haro Objects

Shocks in outflows and jets may produce X-ray emission. Terminal shocks between jets and the interstellar medium, known as "Herbig-Haro (HH) objects", are obvious candidates. Sensitive imaging observations have indeed detected faint X-ray sources at the shock fronts of HH objects (e.g., Pravdo et al. 2001). Shocks may also form inside the jet, close to the driving star. Such X-ray sources have been found close to the class I protostar L1551 IRS5 (Bally et al. 2003; Favata et al. 2002) and the classical T Tauri star DG Tau (Güdel et al. 2008). The faint low-resolution spectra are soft and indicate temperatures of a few million K, compatible with shock velocities of a few 100 km s^{-1}.

8.6 Stellar High-Energy Particles

The elevated activity of the central star may produce high proton fluxes ("stellar cosmic rays") at planetary distances. Feigelson et al. (2002) estimated the proton flux at 1 AU of a solar analog in its T Tauri phase, from a statistical X-ray study of T Tauri stars in the Orion Nebula Cluster. They found that frequent flares on T Tauri stars are $10^{1.5}$ times more luminous than the largest solar flares (or 10^4 times more than solar flares that occur with a daily frequency). These same flares occur at a rate about $10^{2.5}$ higher than the rate of the largest solar flares. As solar proton fluxes scale non-linearly with the solar X-ray luminosity, Feigelson et al. (2002) estimated a proton flux for "T Tauri Sun" about 10^5 times higher than at present (i.e., 10^7 protons cm^{-2} s^{-1} at 1 AU). Given the high flare rate, this flux was probably present almost continuously.

9 Summary

Ionization and heating of gas in protoplanetary disks are primary consequences of high-energy photon and cosmic-ray irradiation. Further processes are involved, such as excitation and molecular dissociation. Chemical networks are driven in particular involving molecular ions, given the high reaction rates of many of them. At the end of the cascade, about 50% of the incoming energy will be transformed into heat.

Only recently has the high-energy radiation from the central star moved into the focus of these mechanisms. X-ray and extreme-ultraviolet radiation is amply available from T Tauri stars, due to

their enhanced magnetic activity levels and strong accretion processes, perhaps even the presence of shocks in winds and outflows. In contrast, cosmic rays may be largely suppressed in the “interesting” regions of a protoplanetary disk, owing to the presence of a strong, magnetized wind akin to the solar wind. For proper disk modeling, it is therefore pivotal to characterize the magnetic activity characteristics of the central star although ionized winds are so far elusive, owing to the lack of measurable diagnostics.

The consequences of disk ionization and heating are far-reaching. While heating leads to photo-evaporation processes in disks at intermediate radii and therefore to the formation of gaps and eventually accelerated dispersion of the entire disk, ionization amplifies the magnetorotational instability leading to enhanced accretion, and therefore also to the disappearance of the disk. Ionization and heating processes are therefore prime actors in the removal of protoplanetary disks, setting critical time limits to the formation of gas giant planets.

Acknowledgments I thank the organizers of our fantastic summer school for providing a relaxing setting and a unique environment for discussing a plethora of disk physical and chemical processes. Christian Rab provided important corrections and comments on the manuscript. This work has been supported by the European Union Seventh Framework Programme FP7-2011 under grant agreement no 284405.

References

Alexander, R. D., Clarke, C. J., & Pringle, J. E. 2004, MNRAS, 354, 71

Alexander, R. D., Clarke, C. J., & Pringle, J. E. 2006a, MNRAS, 369, 216

Alexander, R. D., Clarke, C. J., & Pringle, J. E. 2006b, MNRAS, 369, 229

Aresu, G., Kamp, I., Meijerink, R., et al. 2014, A&A, 566, A14

Aresu, G., Kamp, I., Meijerink, R., et al. 2011, A&A, 526, A163

Balbus, S. A. & Hawley, J. F. 1991, ApJ, 376, 214

Baldovin-Saavedra, C., Audard, M., Güdel, M., et al. 2011, A&A, 528, A22

Bally, J., Feigelson, E., & Reipurth, B. 2003, ApJ, 584, 843

Bethe, H. 1933, in Handbuch der Physik, Vol. 24, 491

Black, J. H. & Dalgarno, A. 1976, ApJ, 203, 132

Calvet, N. & Gullbring, E. 1998, ApJ, 509, 802

Casanova, S., Montmerle, T., Feigelson, E. D., & Andre, P. 1995, ApJ, 439, 752

Clarke, C. J., Gendrin, A., & Sotomayor, M. 2001, MNRAS, 328, 485

Cleeves, L. I., Adams, F. C., & Bergin, E. A. 2013, ApJ, 772, 5

Dalgarno, A., Yan, M., & Liu, W. 1999, ApJ Suppl., 125, 237

Ercolano, B., Clarke, C. J., & Drake, J. J. 2009, ApJ, 699, 1639

Ercolano, B., Drake, J. J., Raymond, J. C., & Clarke, C. C. 2008, ApJ, 688, 398

Favata, F., Fridlund, C. V. M., Micela, G., Sciortino, S., & Kaas, A. A. 2002, A&A, 386, 204

Favata, F., Micela, G., Silva, B., Sciortino, S., & Tsujimoto, M. 2005, A&A, 433, 1047

Feigelson, E. D., Garmire, G. P., & Pravdo, S. H. 2002, ApJ, 572, 335

Fromang, S., Terquem, C., & Balbus, S. A. 2002, MNRAS, 329, 18

Gammie, C. F. 1996, ApJ, 457, 355

Giardino, G., Favata, F., Pillitteri, I., et al. 2007, A&A, 475, 891

Glassgold, A. E., Galli, D., & Padovani, M. 2012, ApJ, 756, 157

Glassgold, A. E. & Langer, W. D. 1973, ApJ, 186, 859

Glassgold, A. E., Najita, J., & Igea, J. 1997, ApJ, 480, 344

Glassgold, A. E., Najita, J., & Igea, J. 2004, ApJ, 615, 972

Gorti, U. & Hollenbach, D. 2004, ApJ, 613, 424

Gorti, U. & Hollenbach, D. 2009, ApJ, 690, 1539

Güdel, M. 2004, A&A Rev., 12, 71

Güdel, M., Skinner, S. L., Audard, M., Briggs, K. R., & Cabrit, S. 2008, A&A, 478, 797

Güdel, M. & Telleschi, A. 2007, A&A, 474, L25

Hartigan, P., Edwards, S., & Ghandour, L. 1995, ApJ, 452, 736

Herczeg, G. J., Najita, J. R., Hillenbrand, L. A., & Pascucci, I. 2007, ApJ, 670, 509

Hollenbach, D., Johnstone, D., Lizano, S., & Shu, F. 1994, ApJ, 428, 654

Igea, J. & Glassgold, A. E. 1999, ApJ, 518, 848

Imanishi, K., Koyama, K., & Tsuboi, Y. 2001, ApJ, 557, 747

Jonkheid, B., Faas, F. G. A., van Zadelhoff, G.-J., & van Dishoeck, E. F. 2004, A&A, 428, 511

Kahn, S. M. 2005, in Saas-Fee Advanced Course 30: High-energy spectroscopic astrophysics, ed. M. Güdel & R. Walter, 3–81

Kastner, J. H., Huenemoerder, D. P., Schulz, N. S., Canizares, C. R., & Weintraub, D. A. 2002, ApJ, 567, 434

Krolik, J. H. & Kallman, T. R. 1983, ApJ, 267, 610

Lepp, S. & McCray, R. 1983, ApJ, 269, 560

Maloney, P. R., Hollenbach, D. J., & Tielens, A. G. G. M. 1996, ApJ, 466, 561

Mamajek, E. E. 2009, in American Institute of Physics Conference Series, Vol. 1158, American Institute of Physics Conference Series, ed. T. Usuda, M. Tamura, & M. Ishii, 3–10

Meijerink, R. & Spaans, M. 2005, A&A, 436, 397

Najita, J. R., Doppmann, G. W., Bitner, M. A., et al. 2009, ApJ, 697, 957

Oppenheimer, M. & Dalgarno, A. 1974, ApJ, 192, 29

Osterbrock, D. E. & Ferland, G. J. 2006, Astrophysics of gaseous nebulae and active galactic nuclei

Owen, J. E., Ercolano, B., & Clarke, C. J. 2011, MNRAS, 412, 13

Owen, J. E., Ercolano, B., Clarke, C. J., & Alexander, R. D. 2010, MNRAS, 401, 1415

Pascucci, I., Hollenbach, D., Najita, J., et al. 2007, ApJ, 663, 383

Pascucci, I., Ricci, L., Gorti, U., et al. 2014, ApJ, 795, 1

Pascucci, I. & Sterzik, M. 2009, ApJ, 702, 724

Pravdo, S. H., Feigelson, E. D., Garmire, G., et al. 2001, Nature, 413, 708

Prisinzano, L., Micela, G., Flaccomio, E., et al. 2008, ApJ, 677, 401

Qi, C., Wilner, D. J., Calvet, N., et al. 2006, ApJL, 636, L157

Rybicki, G. B. & Lightman, A. P. 1979, Radiative processes in astrophysics

Semenov, D., Wiebe, D., & Henning, T. 2004, A&A, 417, 93

Shu, F. H. 1991, The physics of astrophysics. Volume 1: Radiation.

Shull, J. M. 1979, ApJ, 234, 761

Shull, J. M. & van Steenberg, M. E. 1985, ApJ, 298, 268

Spitzer, Jr., L. & Tomasko, M. G. 1968, ApJ, 152, 971

Stelzer, B., Flaccomio, E., Briggs, K., et al. 2007, A&A, 468, 463

Telleschi, A., Güdel, M., Briggs, K. R., Audard, M., & Palla, F. 2007, A&A, 468, 425

Tsuboi, Y., Koyama, K., Murakami, H., et al. 1998, ApJ, 503, 894

Tsujimoto, M., Feigelson, E. D., Grosso, N., et al. 2005, ApJ Suppl., 160, 503

Turner, N. J., Fromang, S., Gammie, C., et al. 2014, Protostars and Planets VI, 411

Walsh, C., Nomura, H., Millar, T. J., & Aikawa, Y. 2012, ApJ, 747, 114

Weisheit, J. C. 1974, ApJ, 190, 735

Wilms, J., Allen, A., & McCray, R. 2000, ApJ, 542, 914